LOAN DOCUMENT

PHOTOGRAPH THIS SHEET

LEVEL

INVENTORY

0

DTIC ACCESSION NUMBER

Kinetics of Supercritical Water Oxidation
QR. Jul 1 - Sep 30, 1996

DOCUMENT IDENTIFICATION

DISTRIBUTION STATEMENT A
Approved for public release;
Distribution Unlimited

DISTRIBUTION STATEMENT

ACCESSION FOR		
NTIS	GRA&I	☑
DTIC	TRAC	☐
UNANNOUNCED		☐
JUSTIFICATION		

BY

DISTRIBUTION/

AVAILABILITY CODES

DISTRIBUTION	AVAILABILITY AND/OR SPECIAL	
A-1		

DISTRIBUTION STAMP

DATE ACCESSIONED

DATE RETURNED

19980710 082

DATE RECEIVED IN DTIC

REGISTERED OR CERTIFIED NUMBER

PHOTOGRAPH THIS SHEET AND RETURN TO DTIC-FDAC

DTIC FORM 70A JUN 90

DOCUMENT PROCESSING SHEET

PREVIOUS EDITIONS MAY BE USED UNTIL STOCK IS EXHAUSTED.

LOAN DOCUMENT

HANDLE WITH CARE

REPORT DOCUMENTATION PAGE

Form Approved
OMB No. 074-0188

1. AGENCY USE ONLY (Leave blank)	2. REPORT DATE 1996	3. REPORT TYPE AND DATES COVERED
		Quarterly Report, July 1 - Sept 30, 1996

4. TITLE AND SUBTITLE

Kinetics of Supercritical Water Oxidation

5. FUNDING NUMBERS

N/A

6. AUTHOR(S)

S.F. Rice, R.R. Steeper, R.G. Hanush. J.D. Aiken, E. Croiset, J.W. Tester, K. Brezinsky

7. PERFORMING ORGANIZATION NAME(S) AND ADDRESS(ES)

Sandia National Laboratories
Combustion Research Facility

8. PERFORMING ORGANIZATION REPORT NUMBER

Case 8610.000

9. SPONSORING / MONITORING AGENCY NAME(S) AND ADDRESS(ES)

SERDP
901 North Stuart St. Suite 303
Arlington, VA 22203

10. SPONSORING / MONITORING AGENCY REPORT NUMBER

N/A

11. SUPPLEMENTARY NOTES

This work was supported in part by SERDP.

12a. DISTRIBUTION / AVAILABILITY STATEMENT

Approved for public release: distribution is unlimited

12b. DISTRIBUTION CODE

A

13. ABSTRACT ***(Maximum 200 Words)***

This project consists of experiments and theoretical modeling designed to improve our understanding of the detailed chemical kinetics of supercritical water oxidation processes. The objective of the four-year project is to develop working models that accurately predict the oxidation rates and mechanisms for a variety of key organic species over the range of temperatures and pressures important for industrial applications. Our examination of reaction kinetics in supercritical water undertakes in situ measurements of reactants, intermediates, and products using optical spectroscopic techniques, primarily Raman spectroscopy. Our focus is to measure the primary oxidation steps that occur in the oxidation of methanol, higher alcohols, methylene chloride, aromatics, and some simple organic compounds containing nitro groups. We are placing special emphasis on identifying reaction steps that involve hydroxyl radicals, hydroperoxyl radicals, and hydrogen peroxide. The measurements are conducted in two optically accessible reactors located at Sandia's Combustion Research Facility (CRF), the supercritical flow reactor (SFR) and the supercritical constant volume reactor, designed to operate at temperatures and pressures up to 600 ^{0}C and 500 MPa. The combination of these two reactors permits reaction rate measurements ranging from 0.1 s to many hours.

14. SUBJECT TERMS	15. NUMBER OF PAGES
Kinetics, Supercritical water oxidation, Supercritical flow reactor, SERDP	38
	16. PRICE CODE N/A

17. SECURITY CLASSIFICATION OF REPORT	18. SECURITY CLASSIFICATION OF THIS PAGE	19. SECURITY CLASSIFICATION OF ABSTRACT	20. LIMITATION OF ABSTRACT
unclass.	unclass.	unclass.	UL

Kinetics of Supercritical Water Oxidation

SERDP Compliance Technical Thrust Area

Quarterly Report

Sandia National Laboratories
Combustion Research Facility
Case 8610.000

Principal Investigator:	Steven F. Rice, Sandia
Project Associates, Sandia:	Richard R. Steeper Russell G. Hanush, Jason D. Aiken,
Visiting Scientist:	Eric Croiset, CNRS Orléans
University Collaborators:	Jefferson W. Tester, MIT Kenneth Brezinsky, U. of Illinois, Chicago Irvin Glassman, Princeton University
Project Manager:	Donald R. Hardesty
Reporting Period:	July 1 - September 30, 1996

Project description

This project consists of experiments and theoretical modeling designed to improve our understanding of the detailed chemical kinetics of supercritical water oxidation (SCWO) processes. The objective of the five-year project is to develop working models that accurately predict the oxidation rates and mechanisms for a variety of key organic species over the range of temperatures and pressures important for industrial applications. Our examination of reaction kinetics in supercritical water undertakes *in situ* measurements of reactants, intermediates, and products using optical spectroscopic techniques, primarily Raman spectroscopy. Our focus is to measure the primary oxidation steps that occur in the oxidation of methanol, higher alcohols, methylene chloride, aromatics, and some simple organic compounds containing nitro groups. We are placing special emphasis on identifying reaction steps that involve hydroxyl radicals, hydroperoxyl radicals, and hydrogen peroxide. The measurements are conducted in two optically accessible reactors located at Sandia's Combustion Research Facility (CRF), the supercritical flow reactor (SFR) and the supercritical constant volume reactor (SCVR), designed to operate at temperatures and pressures up to 600°C and 500 MPa. The combination of these two reactors permits reaction rate measurements ranging from 0.1 s to many hours.

The work conducted here continues the experimental approach from earlier years of this SERDP-funded project by extending measurements on key oxidant species and expanding the variety of experimental methods, primarily spectroscopic in nature, that can be used to examine reactions at SCWO conditions. Direct support is provided to the project collaborators at MIT and Princeton who are contributing to model development for phenol, other aromatics, and halogenated species. These researchers are examining these processes using more conventional sample-and-quench methods.

Executive Summary of Progress this Period

Programmatic

The FY97 Execution Plan was prepared and delivered to the SERDP program office in August. This plan outlines the specific tasks to be accomplished with the anticipated funding for the Sandia, MIT, and Princeton effort.

There were several visiting researchers working on the project this quarter. Melissa Pecullan continued her visit from the previous quarter at Sandia and returned to Princeton September 1. Michael Tucker returned to Brown University in the middle of August. Brian Phenix (MIT) visited for three days in July for discussions on methanol oxidation kinetics and the importance of feed concentration and its effect on the experimentally determined pseudo first-order rate constant.

The Princeton University lead investigator, Ken Brezinsky, has taken a faculty position at the University of Illinois at Chicago. However, Melissa Pecullan will remain at Princeton to complete her Ph.D. thesis on phenol and anisole kinetics. The project continues to support this work at Princeton.

H_2O_2 thermal decomposition

The experimental work on H_2O_2 decomposition was completed and the data has been analyzed. All of the outstanding issues regarding the interpretation of the data have been resolved. The primary breakthrough was realizing that there is a wall-catalyzed decomposition of the feed H_2O_2 in the injector system, and that the amount of feed H_2O_2 that is lost is a strong function of the pressure (and therefore density) of the system. The analysis of the data becomes much simpler within this interpretation. A manuscript is in its final revision stage and will be submitted for publication next quarter.

CO/CO_2 water-gas shift chemistry

A large amount of data was collected this quarter on the water-gas shift chemistry in supercritical water over the pressure range of 1 - 50 MPa (150 -7500 psi) and at temperatures of 410 °C, 450 °C, and 480 °C. The data conclusively show a very strong water-density dependence for the reaction rate at water concentrations above 10 mole/liter. Interestingly, there is only a weak temperature dependence exhibited by the data. These results support the Melius model for the shift reaction in supercritical water. This model postulates that transition states for $CO + H_2O \Rightarrow$ HCOOH (formic acid) and the subsequent decomposition of formic acid to CO_2 and H_2 are stabilized by the direct participation of water in the transition state structures. These experimental results have a direct impact on potential applications to hydrogen production from low-grade fuels.

Massachusetts Institute of Technology, Department of Chemical Engineering

The effort to compare methanol oxidation rates between the MIT and Sandia tubular flow reactors has thus far led to the redesign of the MIT reactor mixing tee and the validation of hydrogen peroxide as an alternative oxidant. While the improvements in mixing lead to better agreement between the methanol oxidation rates observed in both laboratories, the remaining differences were substantial enough to warrant further investigation. Based on an updated Arrhenius plot of the latest MIT and Sandia data, it appears that the two methanol data sets differ by approximately 15 °C. Although this may seem to be small, this difference represents over a factor of two in the measured rate. Experiments are now underway at both laboratories to resolve this small, but still measurable discrepancy.

The investigation of the reaction kinetics of aromatic compounds in supercritical water is currently underway. Several of the partial oxidation products formed during benzene oxidation in supercritical water have been identified. The early appearance of a significant quantity of carbon dioxide relative to the amount of carbon monoxide is in agreement with the observations at the University of Michigan that the carbon dioxide yield always exceeds that of carbon monoxide in the SCWO of phenol, o-cresol and *p*-chlorophenol.

Work has continued on the analysis of methylene chloride (CH_2Cl_2) hydrolysis data gathered last year. The focus has been to account for the significant reaction under subcritical conditions and very little reaction under supercritical conditions. The results will be used to generate a global rate expression for CH_2Cl_2 hydrolysis and oxidation.

Princeton University, Mechanical and Aerospace Engineering Department

The atmospheric pressure pyrolysis and oxidation of anisole have been investigated near 1000 K. This investigation is now complete. Experimental data and pyrolysis modeling results were presented at the Fall Meeting of the Western States Section of the Combustion Institute. In addition, a paper entitled "A Kinetic Study of the Pyrolysis and Oxidation of Anisole" has been submitted to The Journal of Physical Chemistry. The pyrolysis model consists of 66 reversible reactions involving 31 species. Elementary reaction rate parameters for much of the dominant chemistry were obtained from thermodynamic estimations, QRRK analysis, and semi-empirical molecular orbital calculations. Excellent agreement is also obtained between experimental data and model predictions of methylcyclopentadiene and total phenolics. Predictions of benzene and cyclopentadiene, minor species, are reasonable.

Future work

During the next quarter, the work at Sandia will focus on the completion of the water-gas shift measurements, the joint methanol experiments with MIT, and the preparation of several manuscripts for submission to journals. Experiments will begin on measuring the rates of the N_2O disproportionation reaction in the SCVR to initiate the nitrogen chemistry part of the project. We will also conduct a series of experiments on ethanol oxidation to test our theories regarding primary vs. secondary alcohol oxidation rates and to set the stage for calculations and experiments on mixtures. The work at Princeton will focus on completing the publication of the phenol and anisole experimental results and models. The work at MIT will be directed at collecting a detailed data set for benzene oxidation and intermediate product formation rates.

Publications and presentations

Princeton University

M. Pecullan, K. Brezinsky, and I. Glassman, "A Kinetic Study of the Pyrolysis and Oxidation of Anisole", submitted to *The Journal of Physical Chemistry* and presented at the Fall Meeting of the Western States Section of the Combustion Institute.

Detailed Summary of Technical Progress this Period

Sandia Combustion Research Facility

H_2O_2 thermal decomposition

Rate constant derivations

Global kinetics of hydrogen peroxide decomposition are assumed to follow first-order reaction kinetics:

$$-\frac{d\,[H_2O_2]}{dt} = k_g\,[H_2O_2] \qquad (1)$$

where $[H_2O_2]$ is the hydrogen peroxide molar concentration, and k_g the global H_2O_2 decomposition rate constant, in s^{-1}. The rate constant is defined in terms of the experimental measurements by integrating Equation. 1 to yield:

$$\ln\left(\frac{[H_2O_2]_f}{[H_2O_2]_i}\right) = -\,k_g\,t \qquad (2)$$

where t is the residence time and where the indice "i" represents the initial concentration and the indice "f" represents the measured final concentration.

Ordinarily, in our SFR reactor configuration, the initial concentration of hydrogen peroxide is the concentration at the mixing point. Unfortunately, the hydrogen peroxide concentration at the mixing point is not known due to wall-catalyzed decomposition inside the small i.d. injector. As a result, Equation 2 must be written in terms of the known concentration in the H_2O_2 supply vessel, rather than the poorly-defined concentration at the mixing point. Equation 2 is then rewritten in the following form:

$$\ln\left(\frac{[H_2O_2]_f}{[H_2O_2]_0}\right) + \ln\left(\frac{[H_2O_2]_0}{[H_2O_2]_1}\right) + \ln\left(\frac{[H_2O_2]_1}{[H_2O_2]_i}\right) = -\,k_g\,t \qquad (3)$$

where $[H_2O_2]_0$ represents the molar concentration inside the H_2O_2 supply vessel, and $[H_2O_2]_1$ is the hydrogen peroxide concentration at the end of the injector just prior to the mixing point. The first and third terms on the left hand side of Equation 3 are equal to

$$\ln\left(\frac{[H_2O_2]_f}{[H_2O_2]_0}\right) = \ln\left(\frac{\rho_f\,W_f}{\rho_0\,W_0}\right) \qquad (4)$$

and $$\ln\left(\frac{[H_2O_2]_1}{[H_2O_2]_i}\right) = \ln\left(\alpha\,\frac{\rho_1}{\rho_i}\right) \qquad (5)$$

where α is a dilution factor equal to $(F_{hp}+F_w)/F_{hp}$, with F_{hp} and F_w as the hydrogen peroxide and water mass flow rates, ρ is the total density, and W is the hydrogen peroxide mass fraction. With the assumption that $\rho_1 \approx \rho_i \approx \rho_f$, Equation 3, combined with Equations 4 and 5, becomes

$$\ln\left(\alpha\,\frac{\rho_f}{\rho_0}\,\frac{W_f}{W_0}\right) = \ln\left(\frac{[H_2O_2]_f}{[H_2O_2]_i}\right) = -\,k_g\,t + \ln\left(\frac{[H_2O_2]_1}{[H_2O_2]_0}\right) \qquad (6)$$

The left hand side of Equation 6 is determined experimentally. The plot of $\ln(\alpha\rho_F W_F/(\rho_0 W_0)$ vs. time is then a linear function with a slope that represents the rate constant. Here, the concentration $[H_2O_2]_i$ would be the exact value of the initial concentration in the absence of hydrogen peroxide decomposition inside the injector. In that case, the graph obtained from the relationship represented by Equation 6 vs. is a straight line passing through the origin.

Experimental measurements

The first set of measurements were aimed at determining the global hydrogen peroxide decomposition rate constant. As will be seen later, this global rate includes homogeneous decomposition and decomposition due to catalysis by the reactor surfaces. By conducting specific experiments described below that vary the system surface-to-volume ratio, the wall-catalyzed decomposition rate can be separated from the homogeneous process. The rate constants due to wall surface and to homogeneous reactions are treated in the following "Surface Effects" section. This section addresses only the global rate constants.

Experiments were performed at 24.5 and 34.0 MPa for temperatures ranging from 150 to 450 °C. Figures 1 and 2 show the plots of $\ln([H_2O_2]_f/[H_2O_2]_i)$ versus residence time at 24.5 MPa and for temperatures below and above the critical temperature of water (374 °C). The curves obtained are straight lines which confirm that the decomposition of hydrogen peroxide follows Equation 6, and thus follows first order global kinetics. Comparison between these data in these two figures shows important differences between experiments conducted below the critical temperature of water, T_c (374 °C) and above. For experiments below T_c, the straight lines pass through the origin indicating no significant H_2O_2 decomposition inside the injector, whereas above T_c, the straight lines do not pass through the origin implying considerable H_2O_2 decomposition before the mixing point. However, H_2O_2 decomposition inside the injector does not prevent the interpretation of the results because Equation 6 shows that only the slope of the curve is necessary to determine the rate constant. At 34.0 MPa the plots obtained are very similar to those at 24.5 MPa. All rate constants, at different pressures and temperatures, are given in Table 1.

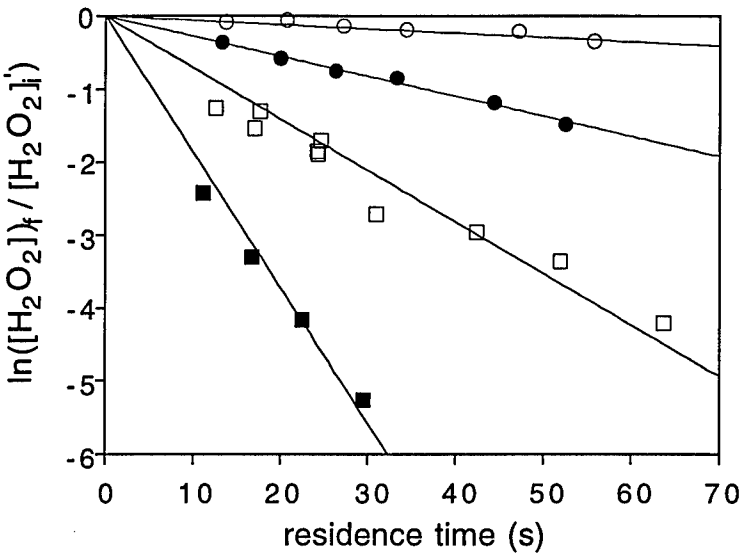

Figure 1 Variation of $\ln([H_2O_2]_f/[H_2O_2]_i)$ versus residence time. Pressure = 24.5 MPa. Results are shown for temperatures below the critical temperature of water: 150 °C ○, 200 °C ●, 250 °C □, 300 °C ■.

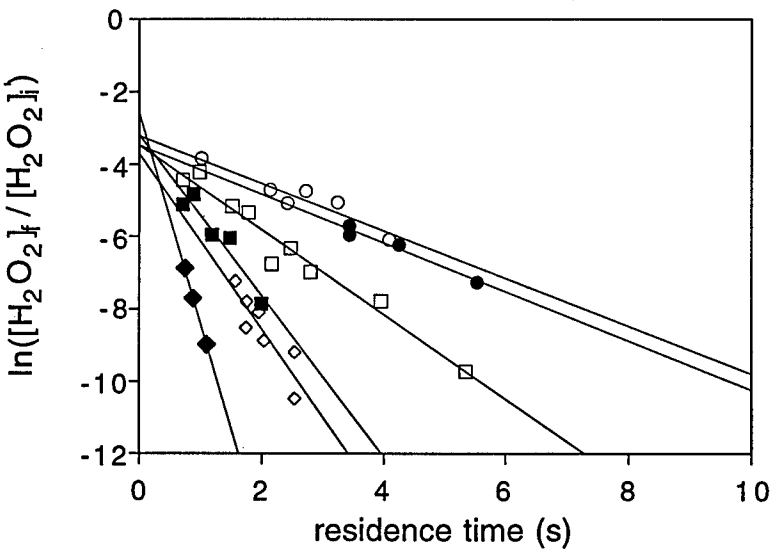

Figure 2 Variation of $\ln([H_2O_2]_f/[H_2O_2]_i)$ versus residence time. Pressure = 24.5 MPa. Results are shown for temperatures above the critical temperature of water: 380 °C ●, 390 °C ○, 400 °C □, 420 °C ■, 425 °C ◇, and 440 °C ◆.

Table 1. Global first order rate constants for hydrogen peroxide decomposition

Press. (MPa)	Temp. (°C)	k (s^{-1})	Press. (MPa)	Temp. (°C)	k (s^{-1})
34.0	180	0.021	24.5	400	1.170
34.0	250	0.106	24.5	420	2.220
34.0	300	0.199	24.5	425	2.420
34.0	350	0.456	24.5	440	5.800
34.0	380	0.480	10.0	330	2.730
34.0	400	0.620	10.0	350	2.510
34.0	425	2.000	10.0	370	2.730
34.0	440	3.840	10.0	390	3.570
34.0	450	5.880	10.0	410	4.200
24.5	150	0.010	5.0	160	0.008
24.5	200	0.030	5.0	200	0.025
24.5	250	0.070	5.0	230	0.049
24.5	300	0.190	5.0	280	2.310
24.5	380	0.680	5.0	300	2.340
24.5	390	0.660	5.0	320	3.080

The Arrhenius plots at 24.5 and 34.0 MPa are presented in Figure 3. This figure shows no measurable differences between global rate constants at 24.5 and 34.0 MPa, below and above the critical temperature of water. Below 374 °C, straight lines are found that confirm that the rate constant follows the Arrhenius form. Above 374 °C, the plot at 34.0 MPa is also a straight line with a slight curvature at the lower temperatures. At 24.5 MPa, the plot is not a straight line and presents a curvature that is more easily observed at temperatures below 420 °C. However, above 420 °C, the plot converges with the plot for the 340 °C data. Considering the straight line obtained at 340 °C, a break in the slope was observed near the critical temperature of water which indicates that the activation energy in the supercritical region is much higher than in the liquid water phase. The regressed expressions of the rate constants are, in the temperature range 150 - 450 °C:

Liquid phase ($T < 374$ °C) $\quad k = 3.3\ 10^{3} \exp(-46{,}100 / RT)$ (7)

Supercritical phase ($T > 374$ °C) $\quad k = 8.2\ 10^{13} \exp(-182{,}000 / RT)$ (8)

In addition, a series of experiments was performed at 5.0 and 10.0 MPa to investigate the behavior of H_2O_2 decomposition below the critical pressure of water (22.1 MPa). The results are shown as an Arrhenius plot in Figure 3. In the liquid phase (for example T < 260 °C at 5.0 MPa), the rate constant is identical to the liquid-phase values at 24.5 and 34.0 MPa. In the gas phase, the Arrhenius plot at 5.0 and 10.0 MPa is much different from the plots under supercritical conditions. The observed rate constants appear to be very weakly dependent on temperature below 370 °C and an increase in the rate constant occurs for temperatures above 370 °C. However, none of the curves obtained at 5.0 and 10.0 MPa follow an Arrhenius form. This observed deviation from an expected Arrhenius behavior originates from surface reactions effects and will be treated below.

In the liquid phase, the rate constant is independent of the pressure when pressure ranges from 5.0 to 34.0 MPa. This can be explained by the fact that water density varies only slightly with pressure in the liquid phase. For example, at 240° C, water density changes from 815 kg m^{-2} at 5.0 MPa to 841.9 kg m^{-2} at 34.0 MPa (NBS Steam Tables, Haar et al., 1984).

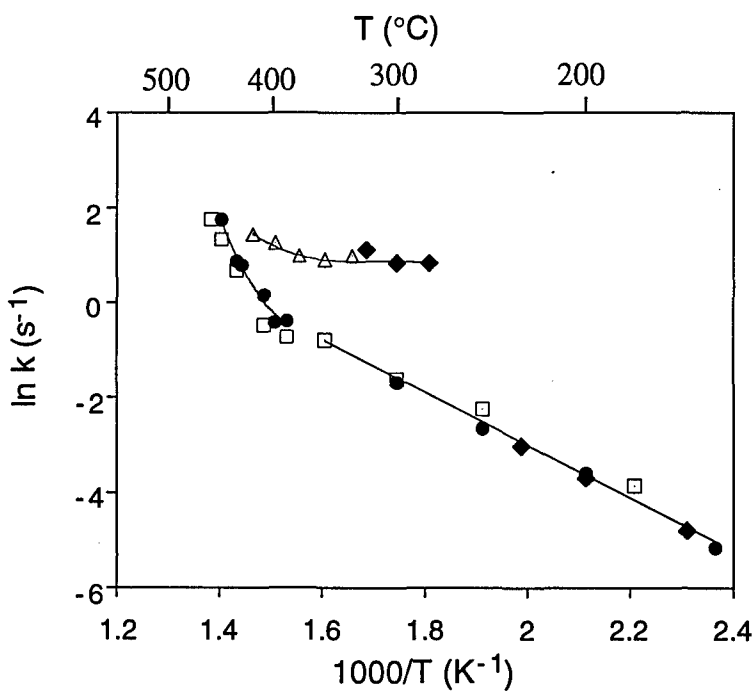

Figure 3 Arrhenius plot of ln (k) versus the reciprocal of the temperature Arrhenius. The rate constants were determined experimentally from the raw data (for example from Figure 2 at 24.5 MPa). The lines are linear fits to data and the curves are polynomial fits to data: 5.00 MPa ◆, 10.0 MPa Δ, 24.5 MPa ●, and 34.0 MPa □.

Surface effects measurements

Hydrogen peroxide is known to be susceptible to decomposition on different surfaces [1]. Surface effects may be important here and thus alter significantly the value of the overall rate constant measured experimentally. To investigate this, experiments were performed at different values of surface-to-volume ratios (S/V).

The original reactor, in which experiments described above were conducted, has an S/V ratio of 8.33 cm^{-1}. To obtain a higher S/V ratio, seven 0.16 cm o.d (1/16 in) Inconel 625 tubes were introduced in the original reactor in a hexagonal configuration. The S/V ratio obtained in that manner is 55.5 cm^{-1}, which corresponds to about seven times higher S/V ratio. An advantage of this method is that, by adding smaller tubes, the surface of the reactor is increased significantly, while the reactor volume decreases only slightly (less than a factor of 1.5). The major change from the previous experiments is then only in the S/V ratio. These experiments were conducted at 24.5 MPa and at temperatures ranging from 300 to 420 °C.

Figure 4 shows the influence of the surface-to-volume ratio on the rate constant when the S/V ratio is increased from 8.3 to 55.5 cm^{-1}. This figure indicates that the slopes, thus the rate constants, are influenced by an increase in S/V ratio. For example, at 410 °C, k increases from 1.4 s^{-1} (at (S/V) = 8.3 cm^{-1}) to 2.9 s^{-1} (at S/V = 55.5 cm^{-1}). The true homogeneous hydrogen peroxide decomposition rate constant would correspond to the experimental rate constant when the S/V ratio approaches zero. Moreover, by assuming that the observed decay constant varies linearly with the S/V ratio, extrapolation to zero S/V will give the homogeneous decomposition rate constant (Holgate and Tester, 1994). Analytically, this method leads to the following expression:

$$k = k_h + k_w \left(\frac{S}{V}\right) \tag{9}$$

where k_h and k_w are rate constants, respectively, for the homogeneous decomposition and for the catalytic decomposition on the wall.

The global heterogeneous decomposition rate can thus be determined as follows :

$$k_w = \frac{(k)_1 - (k)_2}{\left(\frac{S}{V}\right)_1 - \left(\frac{S}{V}\right)_2} \tag{10}$$

where the indices "1" and "2" represent, respectively, experiments run in reactor with low and high S/V ratios. As shown in Figure 5, at supercritical water

conditions, k_w follows the Arrhenius form and the following expressions were determined by linear regression:

$$k_w = 2.0\ 10^3 \exp(-62{,}500 / RT) \qquad \text{for } T \geq T_c \tag{11}$$

$$k_w = 31.0 \exp(-40{,}800 / RT) \qquad \text{for } T < T_c \tag{12}$$

Finally, knowing k_w, the homogeneous rate constant is found to be equal to :

$$k_h = 4.6\ 10^{13} \exp(-180{,}000/RT) \qquad \text{for } T = 380 - 450\ ^\circ C \tag{13}$$

$$k_h = 3.8\ 10^3 \exp(-49{,}00/RT) \qquad \text{for } T = 150 - 350\ ^\circ C \tag{14}$$

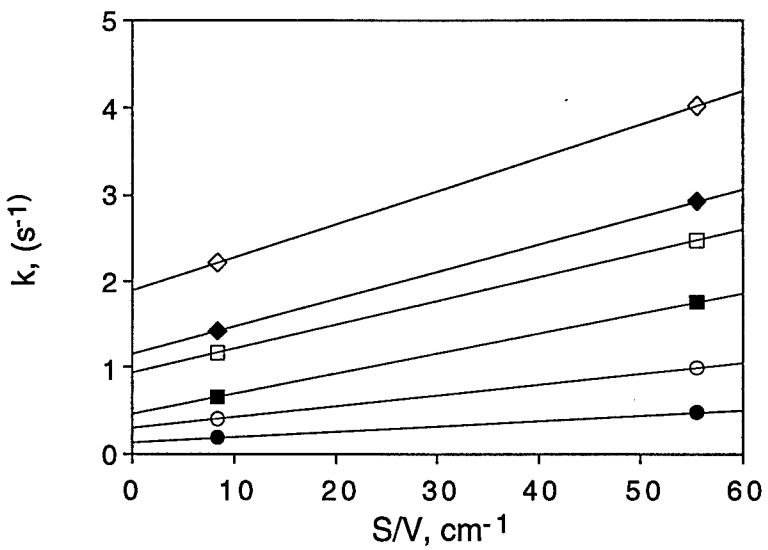

Figure 4 Influence of the surface-to-volume ratio on the decomposition rate constant of hydrogen peroxide. The lines are linear fits to data. Pressure = 24.5 MPa. The different temperatures are: 300 °C ● , 350 °C ○ 390 °C ■ , 400 °C □ , 410 °C ◆ , 420 °C ◇ .

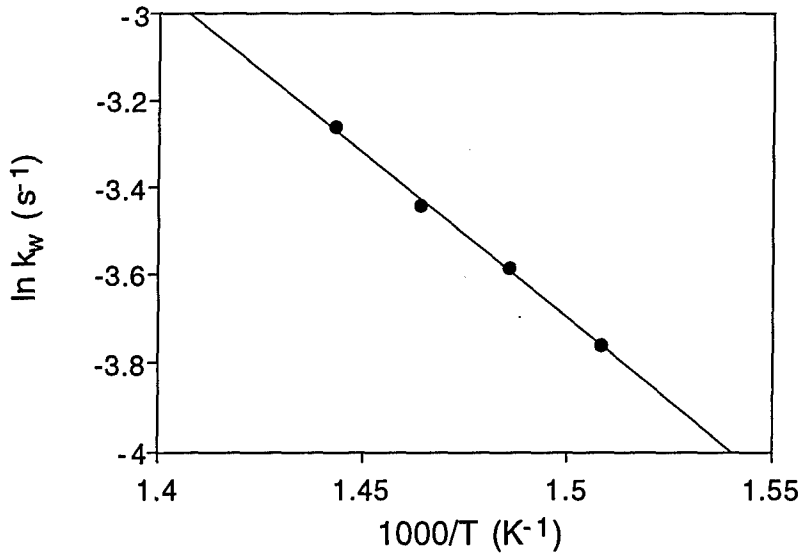

Figure 5 Arrhenius plot of the rate constant for the catalytic H_2O_2 decomposition on the wall surface, P = 24.5 MPa. Temperatures above supercritical temperature of water.

After correction for the surface effect, the rate constant of homogeneous H_2O_2 decomposition in the supercritical water region at 24.5 MPa (see Equation 13) agrees very well with the expression found at 34.0 MPa (see Equation 8). We conclude that the rate constant in the supercritical water region is thus pressure independent. As for the influence of the wall surface at 24.5 MPa and at 400 °C, the rate constant k_w represents 20 % of the global rate constant, whereas at 420 °C its contribution drops to 14 %. At sufficiently high reaction temperatures, the influence of the surface effect will be negligible compared to the homogeneous decomposition rate. However, at temperatures near to the critical temperature of water, the influence of the surface on the global H_2O_2 decomposition rate increases.

On the basis of this analysis we conclude that the curvature observed on the Arrhenius plot at 24.5 MPa (see Figure 3) is due to the increasing importance of the surface effect at lower temperature. Note that the curvature on the Arrhenius plot at 34.0 MPa occurs at lower temperature than at 24.5 MPa, implying that the surface wall effect is less important at 34.0 MPa than at 24.5 MPa. In other words, the influence of surface reactions decreases when the density of the fluid increases. This is consistent with the fact that the collision rate increases with the fluid density relative to collision rate with the surface at higher density.

In the liquid phase, the rate constant described by Equation 14 is very similar to the one without correction from the wall surface, implying that wall surface does not

alter significantly the global rate constant in the liquid phase, again reflecting a decreased influence of surface reactions at liquid higher densities.

Reaction mechanism of H_2O_2 decomposition

Models based on global kinetics do not provide the same predictive capability as models based on verified elementary reaction schemes. The purpose of this section is to determine the rate constant of the elementary reaction of H_2O_2 decomposition, which, as it will be seen, can be derived from the measured global homogeneous rate constant. In the earlier paragraphs, hydrogen peroxide decomposition was described by the global reaction

$$H_2O_2 \xrightarrow{k_g} H_2O + 1/2\, O_2 \qquad (15)$$

It has been suggested [2,3] that this reaction proceeds by the pathway:

$$H_2O_2 + (M) \xrightarrow{k_1} 2\, OH + (M) \qquad (R1)$$

$$OH + H_2O_2 \xrightarrow{k_2} H_2O + HO_2 \qquad (R2)$$

$$OH + HO_2 \xrightarrow{k_3} H_2O + O_2 \qquad (R3)$$

$$HO_2 + HO_2 \xrightarrow{k_4} H_2O_2 + O_2 \qquad (R4)$$

The collision partner in Reaction R1 is H_2O which is in large excess. Moreover, the parentheses surrounding the collision partner in Reaction R1 indicate that at lower pressures the rate for hydrogen peroxide unimolecular dissociation requires a collision. For the densities in the supercritical region, RRKM calculations indicate[4] that the reaction rate is in the high pressure limit and that an increased frequency of collisions does not increase the rate. This hypothesis is strengthened by the results of experiments of Meyer et.al.,[5] who observed that the fall-off region begins at about 2.0 MPa. In addition, rate constants data obtained at 24.5 and 34.0 MPa (see Figure 4) show that these rate constants are independent of the pressure, supporting the fact that the reaction rate is in the high pressure limit in the supercritical region. At the conditions of the present work, the collision partner in Reaction R1 is thus omitted.

The expression for the rate of disappearance of $[H_2O_2]$ is written as:

$$\frac{d[H_2O_2]}{dt} = - k_1 [H_2O_2] - k_2 [OH] [H_2O_2] + k_3 [HO_2]^2 \qquad (16)$$

Using the steady-state assumption for the concentrations of OH and HO_2 we obtain:

$$\frac{d[H_2O_2]}{dt} = - 2 k_1 [H_2O_2] \quad (17)$$

which indicates that the rate measured experimentally is twice the elementary first order rate constant for Reaction R1. The assumption of steady-state for [OH] and [HO_2] was examined using the detailed mechanism for the H-O system and is discussed later in this section.

In the supercritical region the rate constant k_1 becomes

$$k_1 = 2.3\ 10^{13} \exp(-180{,}000/RT) \quad (18)$$

Likewise, in the aqueous phase, the rate constant k_1 is

$$k_1 = 1.9\ 10^{3} \exp(-49{,}000/RT) \quad (19)$$

These values are compared in Table 2 with different rate constants found in the literature. In the aqueous phase the Arrhenius parameters found in the present work are different from those found by Takagi and Ishigure[3]. Yet, the lower activation energy found in this study is counterbalanced by a higher pre-exponential factor. For these two works, the absolute values of the rate constant are found to be of the same order of magnitude in the temperature range 150 - 350 °C. Our results can then be considered in a reasonable agreement with those of Takagi and Ishigure in the aqueous phase.

Considering the state of water in the supercritical region as dense gas, it is meaningful to compare our rate constants in the supercritical region with the high-pressure-limit, second-order rate constants in the vapor phase determined by others. This comparison is shown in Figure 6. The rate constant of Holgate[6] at 24.6 MPa was determined from RRKM calculations and was found to be very close to the high pressure limit rate constant. The values of Baulch et al. [7] extrapolated in Figure 6 to the temperature range 380-450°C, were also determined from RRKM and thus match very well the rate constant determined by Holgate. The rate constants of Meyer et al.[5] are in fact an estimated lower limit of k_∞ and the rate constant of Giguère and Liu is below the high pressure limit.

As seen in Figure 6, the values of Meyer and Giguère are lower than those of the present study. However, the rate constants determined in the present work are significantly higher than the values determined from RRKM calculations. The effect of the wall surface was taken into account in the experimental determination of the rate constant, and thus cannot explain the difference between our rate constants, determined directly experimentally, from those calculated from RRKM theory. This suggests that, on a molecular scale, the nature of H_2O_2 dissociation may be explicitly affected by the presence of water, resulting in additional buffer-concentration dependencies not calculable by way of the RRKM method.

Table 2. Comparison of different values for H_2O_2 thermal decomposition rate constants.

	A	E (kJ mol^{-1})	Temp. range (°C)	Remarks
Supercritical Region				
This work	2.3×10^{13}	180	380 - 450	P = 24.5 - 34.0 MPa
Holgate et al. (1993)	7.8×10^{14}	208.7	400 - 600	P = 24.6 MPa
Vapor phase				
Giguère et al. (1957)	1×10^{13}	201	400 - 500	—
Meyer et al. (1969)	3.2×10^{13}	207	677 - 1177	$k = k_\infty$
Baulch et al. (1994)	3×10^{14}	203	730 - 1230	$k = k_\infty$
Aqueous Phase				
This work	3.8×10^{3}	49	150 - 350	P = 5 - 34 MPa
Takagi et al. (1985)	6.4×10^{5}	71	100 - 250	at least up to 4 MPa[a]

[a]. Maximum operating pressure estimated from water vapor pressure at 250 °C

The determination of k_1 according to Equation 17 supposes steady-state assumption for [OH] and [HO_2]. To check this assumption in the supercritical region, the value of k_1 found in Equation 18 was incorporated in the mechanism presented in Table 3. These calculations were performed within the Chemkin-Real-Gas software package. [8]

The variation of the logarithm of [H_2O_2], [OH] and [HO_2] versus time is shown in Figure 7. The variation of [OH] versus time is strictly zero. The concentration of [HO_2] decreases with time somewhat, however, apparently this rate of change of [HO_2] does not affect the validity of the steady-state assumption. Note that the slope of the straight line, ln[H_2O_2] vs time, is twice the value of k_1, indicating that Equation 17 is satisfied.

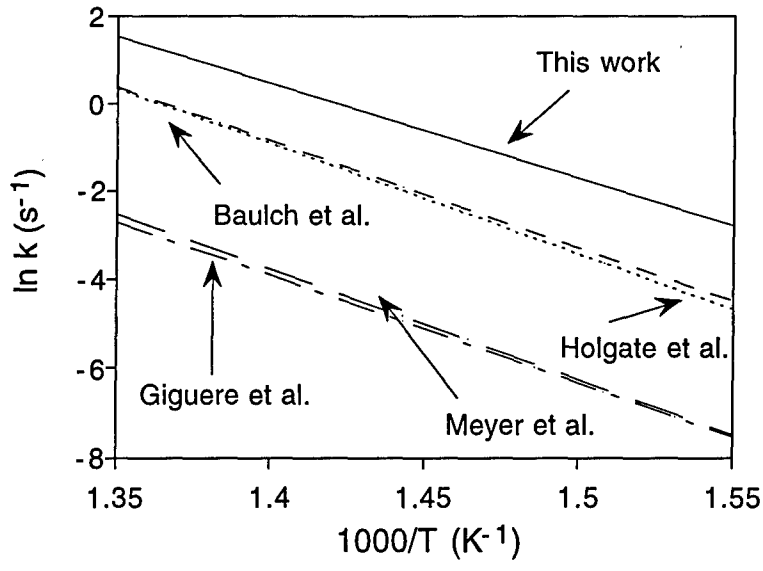

Figure 6 Comparison between different values of rate constants for H_2O_2 thermal decomposition. Holgate's work and the present work correspond to supercritical conditions. The rate constant determined by Baulch et al and Meyer et al. correspond to rates at the high pressure limit, k_∞.

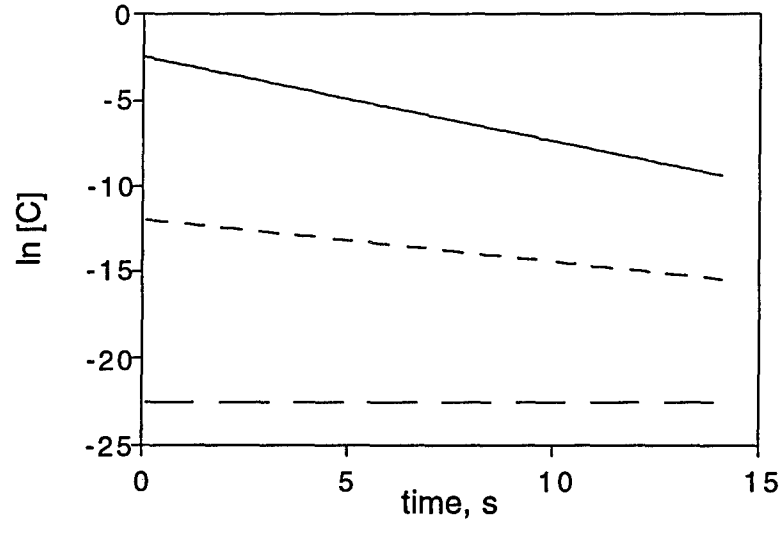

Figure 7 Evolution versus time of the logarithm of H_2O_2, HO_2 and OH concentrations. Calculation done from the mechanism presented in Table 3, T = 400 °C, P = 245 MPa. $[H_2O_2]$ ——— , $[HO_2]$ - - - - - , [OH]— —

Table 3. Detailed reaction mechanism for the O-H system.[a]

	reactions	A	β	T*	Source
1.	$O + H + H_2O \Rightarrow OH + H_2O$	4.71E+18	-1.00	0.0	1
2.	$O + H_2 \Rightarrow H + OH$	5.13E+04	2.67	3160.0	2
3.	$H + O_2 \Rightarrow O + OH$	9.75E+13	0.00	7470.0	3
4.	$O + HO_2 \Rightarrow OH + O_2$	1.75E+13	0.00	-200.0	1
5.	$O + H_2O_2 \Rightarrow OH + HO_2$	9.63E+06	2.00	2000.0	1
6.	$2\,H + H_2 \Rightarrow 2\,H_2$	9.78E+16	-0.60	0.0	3
7.	$H + 2\,O_2 \Rightarrow HO_2 + O_2$	6.41E+18	-1.00	0.0	1
8.	$H + O_2 + H_2O \Rightarrow HO_2 + H_2O$	9.42E+18	-0.76	0.0	4
9.	$H + OH + M \Rightarrow H_2O + M$	2.21E+22	-2.00	0.0	1
10.	$H + HO_2 \Rightarrow O + H_2O$	3.01E+13	0.00	866.0	3
11.	$H + HO_2 \Rightarrow O_2 + H_2$	4.27E+13	0.00	710.0	3
12.	$H + HO_2 \Rightarrow 2\,OH$	1.69E+14	0.00	440.0	3
13.	$H + H_2O_2 \Rightarrow HO_2 + H_2$	1.69E+12	0.00	1890.0	3
14.	$H + H_2O_2 \Rightarrow OH + H_2O$	1.02E+13	0.00	1800.0	3
15.	$H_2 + H_2O \Rightarrow 2\,H + H_2O$	8.43E+19	-1.10	52530.0	1
16.	$OH + H_2 \Rightarrow H + H_2O$	2.16E+18	1.51	1726.0	5
17.	$2\,OH \Rightarrow O + H_2O$	1.52E+09	1.14	50.0	3
18.	$OH + HO_2 \Rightarrow H_2O + O_2$	2.89E+13	0.00	-250.0	3
19.	$OH + H_2O_2 \Rightarrow HO_2 + H_2O$	7.83E+12	0.00	670.0	3
20.	$2\,HO_2 \Rightarrow H_2O_2 + O_2$[b]	5.28E-35	14.06	-9605.0	6
21 a.	$H_2O_2 \Rightarrow OH + OH$[c]	2.28E+13	0.00	21650.0	7
21 b.	$H_2O_2 \Rightarrow OH + OH$	3.00E+14	0.00	24400.0	3
22.	$H_2O_2 \xrightarrow{\text{wall}} H_2O + 1/2\,O_2$	$6.24 \times (S/V)$[d]	0.50	0.0	7

[a] Rate constant = $A\,T^{\beta}\exp(-T^*/T)$ Units of mol, cm^3, s, K. [b] Simplified rate form in the temperature range 673 - 773. [c] determined in supercritical water conditions. [d] In the present work, $S/V = 8.33\ cm^{-1}$. Sources: (1) Tsang and Hampson (1986)[4]; (2) Sutherland et al., (1986)[10]; (3) Baulch et al. (1994)[7]; (4) GRI-Mech 1.2[11]; (5) Michael and Sutherland (1988)[12]; (6) Hippler et al. (1990)[13]; (7) this work.

Surface effects modeling

In the supercritical region it has been seen that surface effects are not negligible in our experimental system, especially for temperatures near the critical temperature of water. The "Surface Effects Measurements" section shows that an empirical rate constant for the reactions of hydrogen peroxide decomposition occurring at the wall surface can be determined. To a first approximation, this rate constant was chosen arbitrarily to be in an Arrhenius form for convenience. Nevertheless, simple kinetic theory of gases gives the following expression for surface reaction rate constant: [9]

$$k_w = \Gamma\left(\frac{S}{V}\right)\sqrt{\frac{kT}{2\pi m}} \qquad (20)$$

where Γ is the efficiency parameter of H_2O_2 removal upon collision with the wall surface, k is the Boltzmann's constant, and m is the mass of an H_2O_2 molecule. Unfortunately, an attempt to fit our data at supercritical conditions into the theoretical expression of Equation 20 failed. In particular, the temperature dependence of our experimental values of k_w, is much greater than can be described by Equation 20. This indicates that the above theoretical expression is not valid at supercritical water conditions for H_2O_2 surface decomposition. Indeed Equation 20 is characterized by a relatively weak temperature dependence: k_∞ is proportional to $T^{1/2}$.

In Figure 4, the data shown in the vapor phase at 5.0 and 10.0 MPa presents a weak temperature dependence. This could be due to a preponderant effect of the surface decomposition over the homogeneous decomposition in the temperature range considered here. To check this possibility, simulation of the gas phase process was done using the Arrhenius plot at 5.0 and 10.0 MPa was done, following the mechanism shown in Table 3 in which the surface effect rate constant (Reaction 22) satisfies Equation 20. The adjustment of the H_2O_2 efficiency parameter to the data at 10.0 MPa leads to the fitted value of $\Gamma = 2.1 \times 10^{-5}$.

The model was investigated by using the rate constant of homogeneous hydrogen peroxide decomposition (reaction R1) found in the present work under supercritical conditions. Comparison of the experimental values with the calculation is shown in Figure 8. This figure shows the transition between decomposition controlled by the surface effects to decomposition controlled by homogeneous reactions. Figure 8 suggests that, under the conditions tested here, the experimental data at 10.0 and 5.0 MPa reflects essentially the hydrogen peroxide decomposition on the wall surface. Comparison between the vapor phase and the supercritical conditions shows that the wall surface decomposition is much more important in the gas phase than in the higher density supercritical phase. For example, the rate constant of the wall effect at 400 °C is 2.8 s^{-1} in the vapor phase (at 10.0 MPa) and 0.03 s^{-1} at supercritical conditions. Apparently, at the higher density supercritical conditions, the efficiency

of the inhomogeneous process is significantly lower, perhaps due to significantly slower diffusion to or from the active sites on the wall. It appears that the same homogeneous process occurs over the pressure range from 5 to 34 MPa. However, experimental limitations, especially due to very fast reactions, prevented us from measuring directly the homogeneous H_2O_2 decomposition rate in the vapor phase at higher temperature.

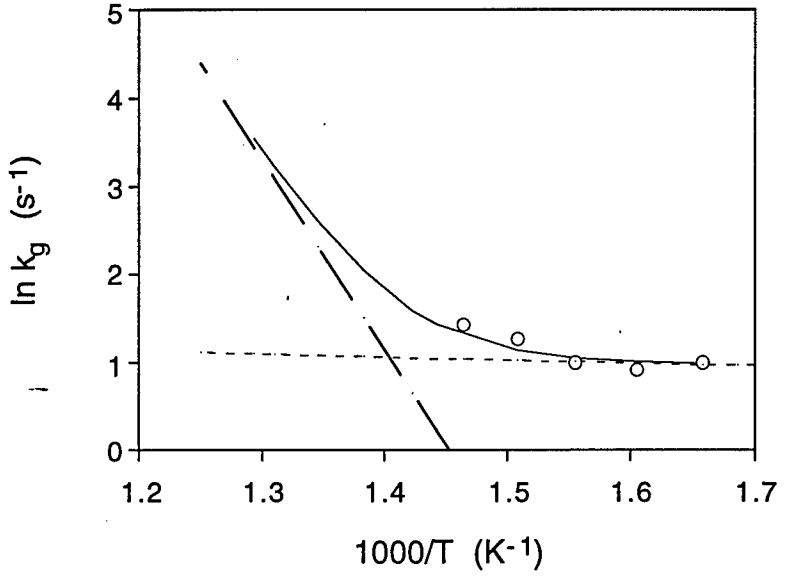

Figure 8 Comparison of the results from the elementary reaction model in Table 3 with the experimental data, Arrhenius plot simulation at 10.0 MPa. The open symbols represent experimental data, and the solid line represents the calculated values of ln k_g. The short dashed line represents ln(2 k_1) and the long dashed line represents ln(k_w) according to Equation 20.

H_2O_2 decomposition and methanol oxidation in SCWO

One of the main motivations of this study is the importance of H_2O_2 decomposition during methanol oxidation in supercritical water.[14] It was found that the model of Schmitt *et al.*[15] reproduces Rice's experimental data fairly well[14] but predicts rates too slow for temperatures below 490 °C. It was also found that, after the induction period, the rate of oxidation of methanol is most sensitive to the rate of the unimolecular dissociation of hydrogen peroxide. We have repeated this calculation with the former expression for the rate of H_2O_2 decomposition replaced by the new expression found in the present work. The new prediction of methanol oxidation behavior was then compared with the former prediction and with the experimental data. This comparison is shown in Figure 9. The new values of the H_2O_2

decomposition rate parameters improve considerably the prediction of the model at 440 and 450 °C, that is in the temperature range of the present work. Extrapolations at temperatures above 450 °C provide good agreement with the experimental data. Yet, at 470 and 490 °C the rate of methanol disappearance is now predicted to be slightly too fast.

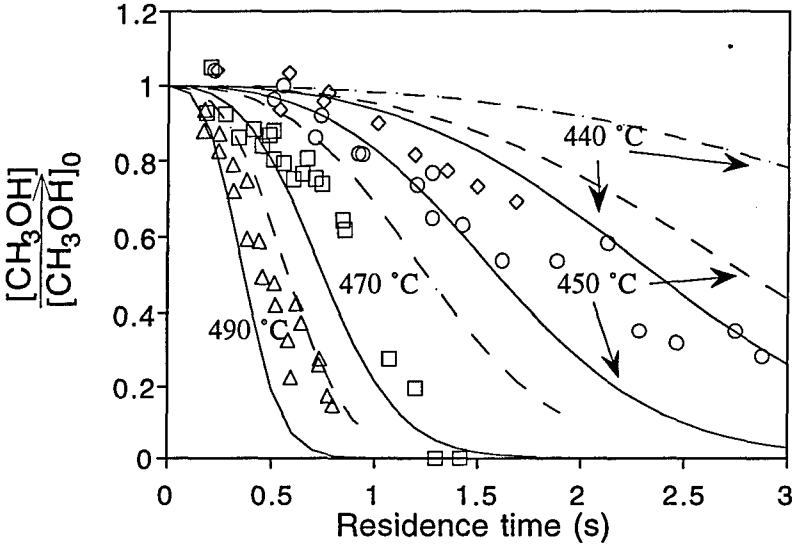

Figure 9 Comparison of experimental results for methanol oxidation in supercritical water (Rice et al., 1996) (open symbol) with the original model of Schmitt et al. (1991) (dotted lines) and with the same model in which H_2O_2 decomposition rate has been replaced by the value determined in the present work (continuous lines). Temperatures: 440 °C ◇ , 450 °C ○ , 470 °C □ , 490 °C △.

H_2O_2 Conclusions

The decomposition rate of hydrogen peroxide is determined experimentally for pressures ranging from 5.0 to 34.0 MPa and temperatures up to 450 °C. It is found that H_2O_2 decomposition in water follows first order kinetics in the aqueous, vapor, and supercritical phases. The homogeneous dissociation rate of hydrogen peroxide was determined independent of the dissociation on the wall surface. The important state variable determining the homogeneous rate of hydrogen peroxide thermal decomposition is the phase. The catalytic decomposition of H_2O_2 at a surface is also determined and is found to vary with water density; its efficiency decreases when the density increases. In the liquid phase, where the density is the highest, the influence of the wall is weak, whereas in the gas phase its influence can be preponderant, especially at low temperatures. Due to higher density, the surface

effect is smaller under supercritical conditions than it is in the high pressure gas phase.

By considering the surface effect, the true homogeneous rate of H_2O_2 decomposition is determined and found to be equal to 2.3 10^{13} exp(-180,000/RT) in the supercritical region at 24.5 and 34.0 MPa. In the temperature range considered here (380 - 450 °C), this rate leads to values higher than those found from RRKM calculations. In addition, result of our experiments conducted in the vapor phase at 5.0 and 10.0 MPa reflect essentially the hydrogen peroxide decomposition on the wall surface, which allows us to determine the corresponding reaction rate based on a simple theoretical expression derived from kinetic theory of gases. However, this theoretical expression fails in describing the wall effect in the supercritical region where an empirical analysis indicates an Arrhenius expression represents the data. Finally, at supercritical water conditions, and for temperatures below 470 °C, the reaction rate for hydrogen peroxide thermal decomposition determined in the present work improves considerably the accuracy of the methanol oxidation model studied by Rice *et al.* (1996).[14]

CO/CO_2 water-gas shift chemistry

An important aspect of modeling reactions in supercritical water, especially from a combustion chemistry perspective, centers on the issue of whether the reaction chemistry involves the specific participation of water. It is possible that the presence of high density water enables individual elementary reactions to proceed at rates that are significantly different from those that would be predicted from a simple extrapolation of gas phase expressions to higher pressure. There are a number of ways that water can affect the rate of a reaction under these conditions. These are:

1) React directly Reactions such as $H_2O + CH_3 => CH_4 + OH$ are directly dependent on water concentration. If such a reaction were rate controlling for methane oxidation, for example, we would expect the overall oxidation rate to reflect a dependence on water concentration relative to an inert species such a argon. Evidence for such an effect has been observed for methane oxidation.

2) Participate as a collision partner in "unimolecular" reactions Reactions that are formally unimolecular such as the decomposition of hydrogen peroxide into hydroxyl radicals, $H_2O_2 + [M] => 2\ OH + [M]$; $M = H_2O$ require a collision partner in the gas phase to supply the energy to the reaction. In the Lindemann transition state model, these reactions become independent of [M] at higher densities.

3) Restrict diffusion controlled reactions Several of the reactions in elementary gas-phase models in supercritical water are evaluated to be very fast when assuming that collisions occur at the gas kinetic rate. At higher concentration of reactants, the rate determining step in facilitating these reactions is not the energetic term in the transition state model, but is the rate at which the species can be brought together.

That is to say, the gas kinetic collision rate overestimates the actual collision frequency due to a finite diffusion rate in the supercritical fluid. To date, little work has been focused on this possible rate limiting effect.

4) Modify transition states The activation energy associated with the activated complex in an elementary reaction can be significantly changed by the presence of additional molecules nearby. This can occur either by direct participation, in this case, of water, in the structure of the transition state or by stabilizing (or destabilizing) the overall activated complex through electrostatic forces as a solvent at these high densities.

5) Change equilibrium of reactants and products At high densities, the nonideality of the fluid can affect the total free energy of the system relative to the values in the gas phase through solvent-like electrostatic effects, as in 4) above. This especially a possibility for a polar species such as water.

Several years ago, Melius et al.[16] conducted a theoretical investigation of the homogenous gas-phase water-gas shift mechanism. They suggested that, at sufficiently high water densities, the activation energies for the two-step process of CO conversion to formic acid and the subsequent decomposition of formic acid to CO_2 and H_2 is significantly stabilized by the participation of additional water molecules in the transition state complex. We have examined the conversion of CO and H_2O to CO_2 and H_2 in the absence of a catalyst in supercritical water over a range of conditions from 400 - 500 °C and 2.0 - 50 MPa, in our optically accessible constant-volume reactor (SCVR). We employed Raman spectroscopy as an *in situ* real-time diagnostic for measuring reaction rates. This diagnostic permits the continuous monitoring of CO, CO_2 and H_2 concentrations as the reaction proceeds.

The data conclusively show a very strong water-density dependence for the reaction rate at water concentrations above 10 moles/liter. Interestingly, there is only a weak temperature dependence exhibited by the data. Figure 10 shows an example of the progress of the reaction in supercritical water at 410 °C and 26.8 MPa (3900 psi). At these conditions the water concentration is 9.4 mole/l. The reaction is extremely slow and the carbon balance is essentially complete considering only CO and CO_2. The first order rate constant determined from $d\ln[CO]/dt$ is about 7.5×10^{-5} s^{-1}. Figure 11 shows the progress of the reaction at 51.7 MPa (7500 psi) (water concentration = 30.8 mole/l). The effective first order rate constant is 3.0×10^{-3} s^{-1}. A change in water concentration by a factor of 3 results in a change in the rate by a factor of 40.

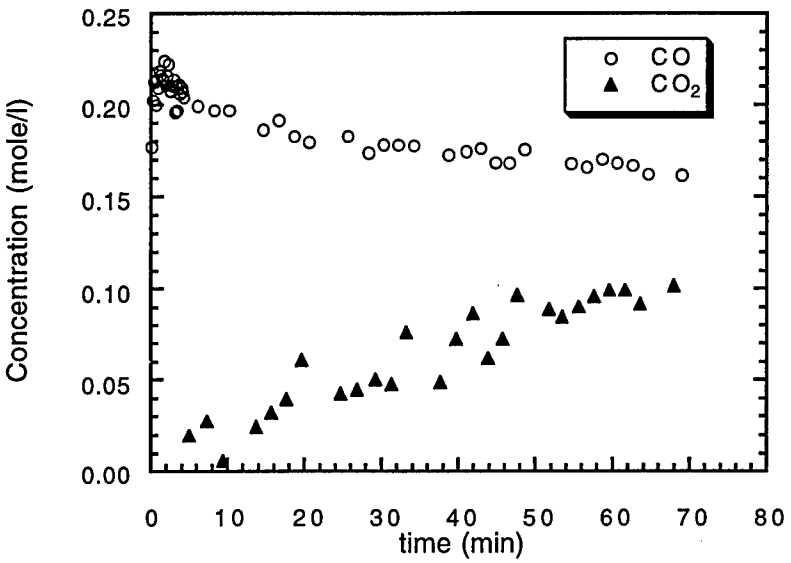

Figure 10 Concentration of CO and CO_2 as a function of time at 3900 psi an 410 °C in supercritical water.

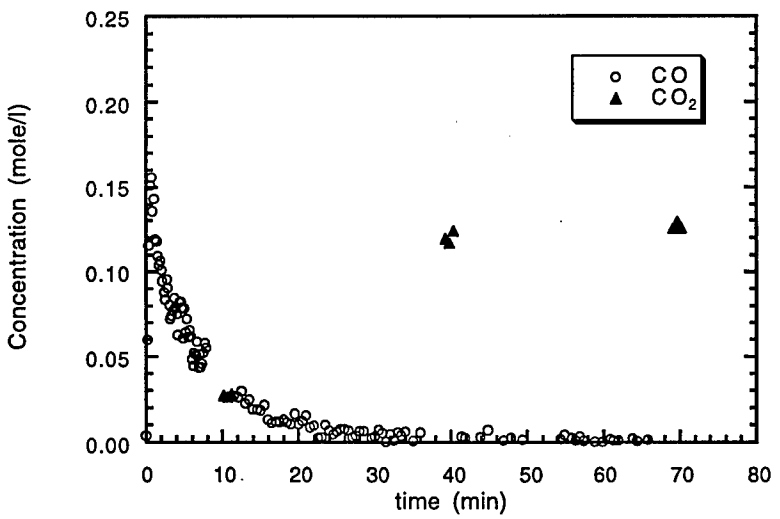

Figure 11 Concentration of CO and CO_2 as a function of time at 7500 psi an 410 °C in supercritical water.

There are two important observations: 1) we have observed an increase in the reaction rate over a range of temperatures when the density of water is raised above 0.35 g/cm^3 that is much greater than a linear dependence on the water concentration, and 2) at elevated pressure and temperature, the conversion of CO is complete. The analysis of these data within the context of the Melius model suggests that densities above the critical density of water afford a change in the homogenous water-gas shift mechanism that results in rapid and complete conversion in a catalyst -free single processing step.

Figure 12 shows the results of all of the experiments recorded to date at 410 °C, 450 °C, and 480 °C. With the rate constant k defined as k= -dln[CO]/dt. The data is close to first order in CO concentration over the entire pressure range that was examined. Although typically the consumption of the first 30 % of the CO does generally appear to be slightly faster than at later times. However, because the rates vary approximately two orders of magnitude over the experimental pressure range, in order to compare all of the results together, the later time (slower) rate constant is presented.

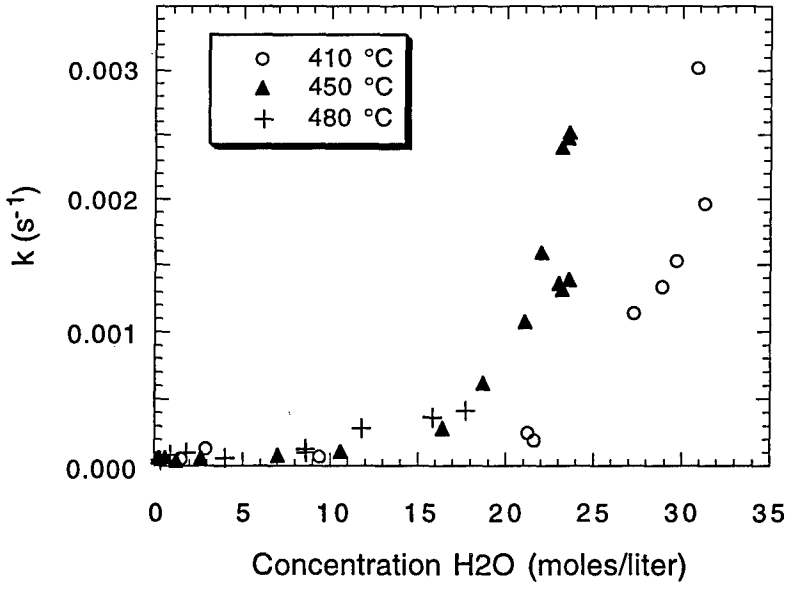

Figure 12 First order rate constant, defined as -dln [CO]/dt, plotted as a function of water concentration at 410 °C, 450 °C and 480 °C.

Clearly, there is a significant non-linear variation in the conversion rate of CO to CO_2 as a function of water concentration. Figure 13 shows these data plotted on a semi-log plot. This shows that the variation with water concentration is not linear over the entire experimental regime. These data strongly support the suggestion by

Melius et. al. that the transition states for the formation and decomposition of the formic acid intermediate are significantly different at the higher water densities. At this time we are still in the process of collecting data at higher temperature and at pressure. A more complete analysis of these data will be presented in our next quarterly report.

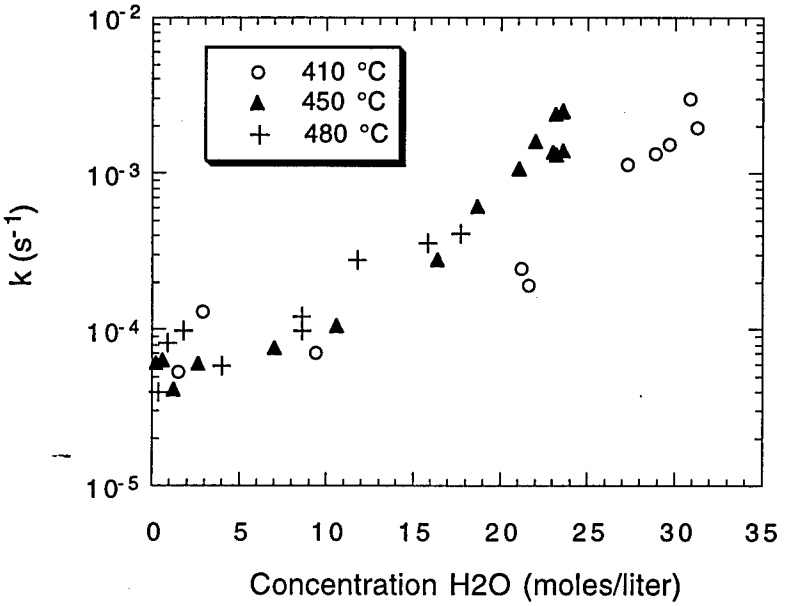

Figure 13 Same data in Figure 12 replotted in semi-logarithmic format.

Massachusetts Institute of Technology, Department of Chemical Engineering

This work was supported partly by the Sandia (SERDP) program and partly by the ARO URI (Army Research Office University Research Initiative) program.

Comparison of SCWO Methanol Kinetics.

The effort to compare methanol oxidation rates between the MIT and Sandia tubular flow reactors has thus far led to the redesign of the MIT reactor mixing tee and the validation of hydrogen peroxide as an alternative oxidant. While the improvements in mixing led to better agreement between the methanol oxidation rates observed in both laboratories, the remaining differences were substantial enough to warrant further investigation. Based on the results of a simple preheater control experiment, we felt that a systematic temperature measurement error in the MIT system might be responsible, as highlighted in our last quarterly report.

Interest in closing the gap between the two methanol data sets resulted in a very productive three-day visit of an MIT researcher, Brian Phenix, to Sandia in July. A review of the data and work with a Sandia methanol oxidation model led to two conclusions. First, the current approach of comparing rate constants derived from both high- and low-conversion experiments is inadequate due to the presence of an induction time in the data. The observed induction time or lag makes the calculated rate constants dependent on the extent of reaction. To date, the bulk of MIT data have been taken at low to moderate conversions (typically 20-70%) while the Sandia data being used in the comparison have been from relatively high conversion experiments (70-95%). It was agreed that a series of new, jointly-planned experiments should be carried out at both laboratories and the basis for comparison should be the raw data rather than derived quantities such as rate constants.

Improvements to the SCWO Reactor System.

Based on an updated Arrhenius plot of the latest MIT and Sandia data, it appears that the two methanol data sets differ by approximately 15 °C. As a result of the possible temperature discrepancy, efforts have been ongoing at MIT to improve the feed stream preheating system to minimize heat loss between the preheater section and the main reactor. We have successfully designed, installed, and tested a direct ohmic preheating system which enables us to provide power input throughout the entire length of the preheating transfer lines. We have also doubled the length of preheater tubing immersed in the main sandbath to provide sufficient residence time at reaction temperature to make up for any heat loss in the transfer lines. After these modifications, a series of experiments were carried out to ensure that the additional preheating lines did not interfere with fluidization in the sandbath. Those experiments demonstrated that there were no dead zones or significant temperature variations in the main sandbath. Experiments are now underway with the modified system. The goal, as before, is to carry out methanol oxidation experiments under identical operating conditions to those used at Sandia.

Oxidation kinetics of aromatics in supercritical water.

The investigation of the reaction kinetics of aromatic compounds in SCW is currently underway. The immediate goal of the research on aromatics, which will continue to be the main focus of research under the SERDP program in the year ahead, is to gather kinetic data on the oxidation of benzene and phenol. We are using the bench-scale, tubular flow reactor to measure the rates and extents of benzene and phenol disappearance as functions of temperature, pressure (or density), and the inlet oxygen and aromatic concentrations. The intent is to represent this data using global kinetic rate expressions that correlate the reaction rates of benzene and phenol in SCW to the feed concentrations and temperature.

Analysis of benzene and its partial and final oxidation products is being conducted using gas chromatography (GC) with both flame-ionization (FID) and thermal conductivity (TCD) detectors. Analysis of low molecular weight, gas-phase hydrocarbons is performed by GC-FID with a 30m x 0.32 mm Astec GasPro™ capillary column. Permanent gases (oxygen, nitrogen, hydrogen, carbon monoxide, and carbon dioxide) are analyzed by GC-TCD using a 5' x 1/8" OD packed Carboxen 1000 column connected via an air-actuated switching valve with a 8' x 1/8" OD Molesieve 5A column. Analysis of liquid samples for benzene and phenol is conducted by GC-FID on a 30 m x 0.53 mm Supelco SPB-1 capillary column preceded by a 2.5 m x 0.53 mm Restek Hydroguard™ column .

The partial oxidation products formed during benzene oxidation in SCW which have thus far been identified by the above-mentioned GD-FID and GD-TCD analysis appear in Figure 14-16. Carbon balances (moles of carbon recovered in products/moles of carbon in feed) calculated using only the species appearing in Figure 14 range from 90-105%, indicating that these products account for the majority of the reacted carbon. Of these products, most of the reacted carbon is in the form of carbon monoxide, carbon dioxide, phenol and methane. Ethylene and acetylene each account for less than 1% of the reacted carbon. The early appearance of a significant quantity of carbon dioxide (Figure 1) relative to the amount of carbon monoxide is in agreement with the observations at the by Savage and co-workers at the University of Michigan that the carbon dioxide yield always exceeds that of carbon monoxide in the SCWO of phenol, *o*-cresol and *p*-chlorophenol.

Efforts are underway to identify the remaining minor partial oxidation products. The pH of the liquid effluent from benzene oxidation experiments is typically around 4, signifying the presence of small amounts of organic acid(s). The gas-phase analysis by GC-FID shows that there are several yet unidentified compounds present, although also in small amounts. Additionally, it is possible that minute amounts of higher molecular weight condensation products are being formed during the SCWO of benzene since they were observed in the effluent from SCWO experiments of aromatics by Savage and co-workers. There are a variety of analytical techniques available to us at MIT which we intend to exploit to identify these remaining minor partial oxidation products, including GC-MS and HPLC coupled with both mass spectrometry and diode array detection.

Experiments are continuing on benzene oxidation in SCW to complete our goal of developing a regressed global rate expression. We will be comparing the experimental species concentration profiles of benzene as well as of the partial and final oxidation products with those obtained using a benzene combustion model developed at MIT, which has been adjusted for high pressure, to determine if the mechanism for benzene oxidation in SCW is similar to that under combustion conditions. Following these experiments with benzene, complementary experiments will be performed using phenol, which we observe as an intermediate in the SCWO of benzene (see Figure 15), as well as with other select aromatics.

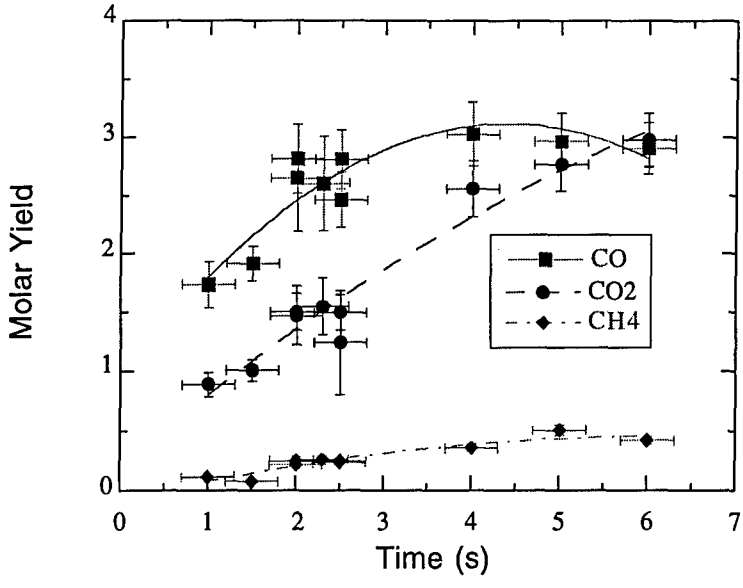

Figure 14 CO, CO_2 and CH_4 produced during SCWO of benzene, (575±4°C, 246±2 bar, 7.5:1 O_2/C_6H_6 Molar Feed Ratio). Molar yield is defined as the mole of product/mole of benzene reacted.

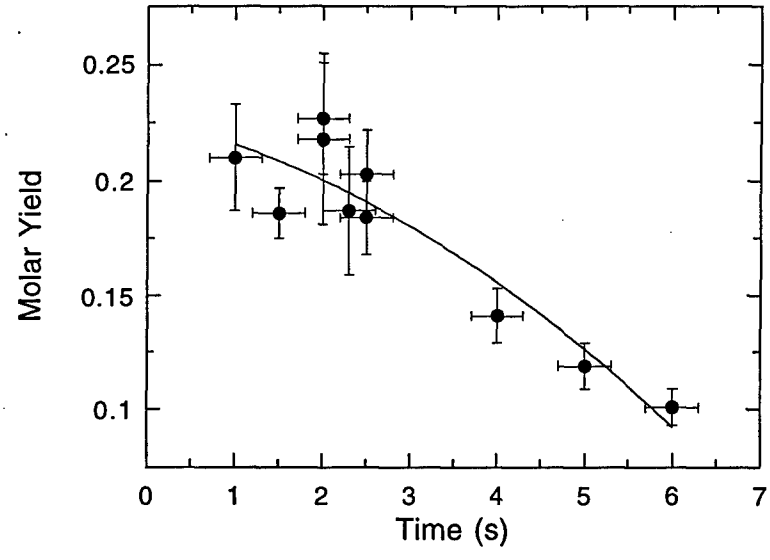

Figure 15 Phenol produced during SCWO of benzene (575±4°C, 246±2 bar, 7.5:1 O_2/C_6H_6 Molar Feed Ratio).

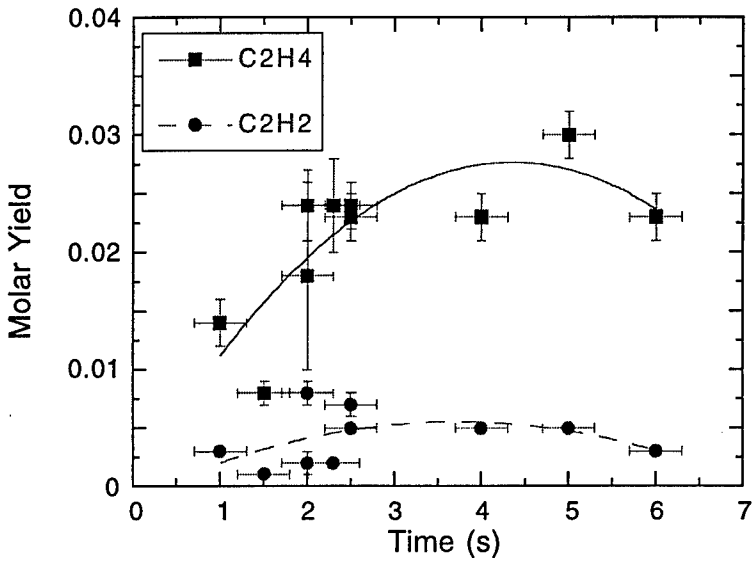

Figure 16 Minor species acetylene and ethylene produced during SCWO of benzene (575±4°C, 246±2 bar, 7.5:1 O_2/C_6H_6 Molar Feed Ratio).

Hydrolysis of CH_2Cl_2 in Sub- and Supercritical Water.

Work has continued on the analysis of methylene chloride (CH_2Cl_2) hydrolysis data gathered last year. The focus has been to account for the significant reaction under subcritical conditions and very little reaction under supercritical conditions. The results will be used to generate a global rate expression for CH_2Cl_2 hydrolysis and oxidation.

An extensive literature search was conducted to find heat transfer correlations for water under sub- and supercritical conditions. These correlations were needed to model the temperature-time history of the feed solution in the preheater tubing. More than one correlation was needed to account for the different physical and geometric conditions that exist at different positions in the preheater tubing. Together these correlations allow calculation of the internal heat transfer coefficient and take into account the following: flow regime (laminar or turbulent), tube orientation (horizontal or vertical), direction of flow (up or down for vertical orientation), the presence of mixed convection (forced and natural), heat transfer effects near the critical point, and the lowering of the transition to turbulence under conditions where natural convection is significant; all developed for water. The fact that the preheater tubing is coiled was found not to have a significant effect on heat transfer due to the relatively large radius of coiling (13 cm) compared to the tubing diameter (1 mm). The constant external heat transfer coefficient was fit to

the experimental data so as to match the measured temperature at the end of the preheater tubing. The fitted values were found to be in very good agreement with what would be expected for tubing in a fluidized sandbath under these conditions.

These heat transfer coefficient values were used in a differential heat balance (all encoded in a Fortran program) to predict the temperature and time profiles as a function of position in the preheater tubing. These profiles have helped us to explain some of the unusual trends observed in experimental conversion values, and to correctly predict high, but subcritical, temperatures (where materials are most susceptible to corrosion) at positions where corrosive failure actually occurred in the preheater tubing.

The fact that hydrolysis conversion of CH_2Cl_2 was very low under supercritical conditions is actually not that surprising when one considers the effects on this reaction of the changing nature of the water environment as temperature increases. The transition state complex formed from the reaction of CH_2Cl_2 and H_2O is more polar (higher charge density) than either of the two neutral reactants. Therefore, a decrease in the water solvent polarity (as occurs with increasing temperature near the critical point and beyond) results in less stabilization of the transition state and consequently a slower reaction rate relative to that in lower temperature liquid water.

To quantify this effect, one needs to incorporate a correction factor into the standard Arrhenius form of the reaction rate constant. This correction factor is based on the change in the Gibbs free energy, ΔG, involved in transferring a molecule from a medium of dielectric constant $\varepsilon=1$ (vacuum) to a medium of dielectric constant ε, and can be derived from a combination of electrostatics and transition state theory. The actual form of the correction factor depends on the dielectric constant and temperature of the medium, as well as the dipole moment (μ) and radius (r) of both reactants and the transition state complex.

We have are currently using *ab initio* calculations to determine μ and r for CH_2Cl_2, H_2O, and their transition state. So far, the calculations are in good agreement and confirm our expectations. They do show a much higher μ or charge density derivative for the transition state as expected and predict that the value of the rate constant at 550°C should drop by more than two natural log units due to the decreasing polarity of water under these conditions. Future work will involve using this correction factor for the rate constant in a nonlinear regression of our experimental data to determine optimized Arrhenius parameters for both CH_2Cl_2 hydrolysis and oxidation.

Finally, we are beginning some batch experiments on CH_2Cl_2 hydrolysis to determine if there is any catalytic effect due to the Hastelloy C-276 tube wall. These experiments will be conducted over the subcritical range of 100-300°C, where most of the reaction probably occurs. The experiments will be performed in a series of glass ampules; one containing only CH_2Cl_2 solution and one or more others containing

various amounts of nickel alloy (Hastelloy C-276 or Inconel 625) beads. The results will help us to determine if there is any significant effect of nickel alloy on CH_2Cl_2 breakdown (relative to the homogeneous reaction), and allow us to compare and extend the range of a similar earlier study found in the literature that was done in Pyrex ampules only at low temperature (80-150°C) and without any nickel alloy present.

Princeton University, Mechanical and Aerospace Engineering Department

As reported previously, the atmospheric pressure pyrolysis and oxidation of anisole have been investigated near 1000 K. Experimental data and pyrolysis modeling results were presented at the Fall Meeting of the Western States Section of the Combustion Institute. In addition, a paper entitled "A Kinetic Study of the Pyrolysis and Oxidation of Anisole" has been submitted to The Journal of Physical Chemistry.

The pyrolysis model consists of 66 reversible reactions involving 31 species. Elementary reaction rate parameters for much of the dominant chemistry were obtained from thermodynamic estimations, QRRK analysis, and semi-empirical molecular orbital calculations. Model predictions of anisole decay and CO production, descriptors of overall reaction progress, agree well with experiment (Figure 17). Excellent agreement is also obtained between experimental data and model predictions of methylcyclopentadiene (Figure 18) and total phenolics (Figure 19). Predictions of benzene and cyclopentadiene, minor species, are reasonable (Figure 18). The model presently does not predict well the production of phenol. Total phenolics are successfully modeled, but the split between phenol and cresols is not. At longer residence times, phenol constitutes approximately half the measured yield of phenolics. In contrast the model overpredicts cresols by a factor of 2 and, essentially, does not predict phenol. Accordingly ethane and methane are underpredicted; methyl groups are trapped in excess cresols, unavailable to reactions forming methane and ethane.

A model for the oxidation of anisole is currently under development. As reported previously, oxidation is observed to proceed through the methylcyclopentadiene molecule. Rate parameters for reaction steps involving the addition of radicals (H, HO_2, O) to $CH_3C_5H_5$ and subsequent ring rupture have been estimated from analogous reactions and thermodynamic considerations. The modeling of methylcyclopentadiene oxidation is complicated by the presence of all three of its isomers. Two are observed experimentally and the presence of the third is inferred from knowledge of the $CH_3C_5H_5$ formation pathways in the anisole system. Thus far, the oxidation model accounts qualitatively for the C_2-C_4 reaction intermediates observed in the oxidation of anisole.

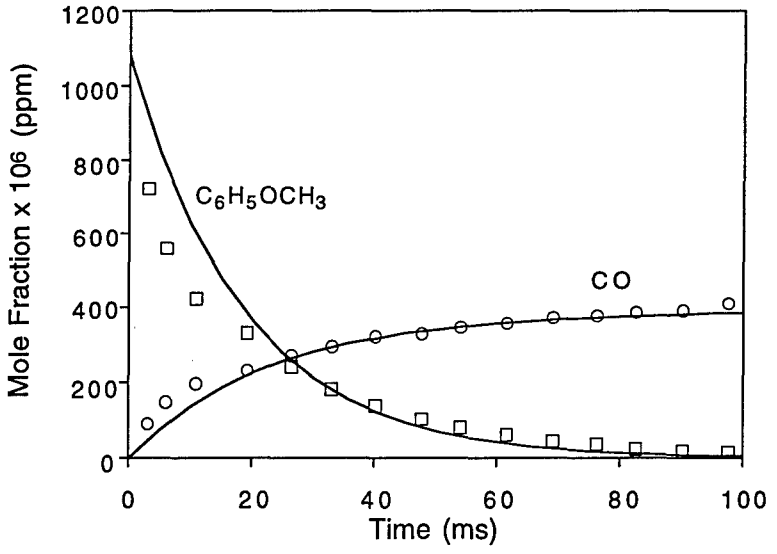

Figure 17 Comparison of experimental data and model prediction of anisole and carbon monoxide. Solid lines indicate model results.

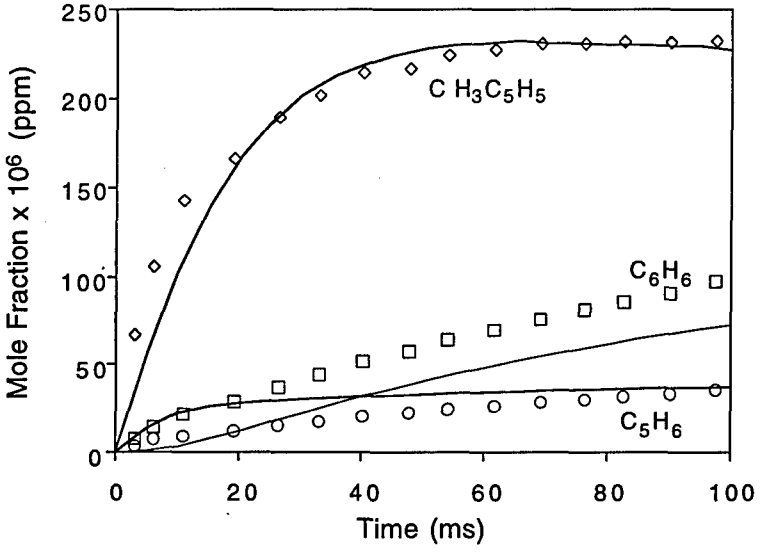

Figure 18 Comparison of experimental data and model prediction of cyclopentadiene, methylcyclopentadiene, and benzene. Solid lines indicate model results.

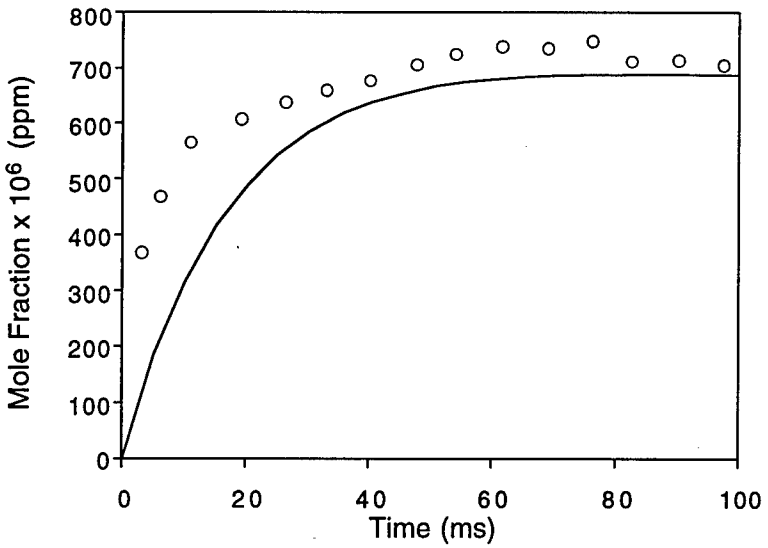

Figure 19 Comparison of experimental data and model prediction of total phenolics=phenol+o- and p-cresols. Solid line indicates model results.

Development of the anisole oxidation model will continue toward quantitative prediction of the consumption of methylcyclopentadiene and the production of C_2-C_4 hydrocarbons and CO. The development of a phenol model is also planned based upon data collected last year for the oxidation of phenol over a range of stoichiometries at 1170 K.

References

1 D. E. Cheaney, D. A. Davies, A. Davis, J. B. Hoare, J. B. Protheroe, and A. D. Walsh, in *Seventh Symposium (International) on Combustion.* (Butterworths, London, 1959), p. 183.

2 P. A. Giguère and I. D. Liu, *Can. J. Chem.* **35,** 283-293 (1957).

3 J. Takagi and K. Ishigure, *Nuclear Science and Engineering* **89,** 177-186 (1985).

4 W. Tsang and R. F. Hampson, *Journal of Physical and Chemical Reference Data* **15,** 1087-1279 (1986).

5 E. Meyer, H. A. Olschewski, J. Troe, and H. Wagner, in *Twelveth Symposium (International) on Combustion* (The Combustion Institute, Pittsburgh, 1969), pp. 345-355.

[6] R. H. Holgate, Ph.D. Thesis , Massachusetts Institute of Technology, 1993.

[7] D. L. Baulch, C. J. Cobos, R. A. Cox, P. Frank, G. Hayman, T. Just, J. A. Kerr, T. Murrells, M. J. Pilling, J. Troe, R. W. Walker, and J. Warnatz, *J. Phys. Chem. Ref. Data* **23,** 847-1033 (1994).

[8] M. K. Alkam, V. M. Pai, P. B. Butler, and W. J. Pitz, *Combustion and Flame* **106,** 110-130 (1996).

[9] D. E. Hoare, G. B. Peacock, and G. R. D. Ruxton, *Trans. Faraday Soc.*, **63,** 2498-2503. (1967).

[10] J. W. Sutherland, J. V. Michael, and R. B. Klemm, *Journal of Physical Chemistry* **90,** 5941-5945 (1986).

[11] M. Frenklach, H. Wang, C.-L. Yu, M. Goldenberg, C. T. Bowman, R. K. Hanson, D. F. Davidson, E. J. Chang, G. P. Smith, D. M. Golden, W. C. Gardiner, and V. Lissianski, http://www.gri.org (1995).

[12] J. V. Michael and J. W. Sutherland, *Journal of Physical Chemistry* **92,** 3853-3857 (1988).

[13] H. Hippler, J. Troe, and J. Wilner, *Journal of Chemical Physics* **93,** 1755-1760 (1990).

[14] S. F. Rice, T. B. Hunter, Å. C. Rydén, and R. G. Hanush, *Industrial and Engineering Chemistry Research* **35,** 2161-2171 (1996).

[15] R. G. Schmitt, P. B. Butler, N. E. Bergan, W. J. Pitz, and C. K. Westbrook, in *1991 Fall Meeting of the Western States Section/The Combustion Institute* (University of California at Los Angeles, CA, 1991), pp. 19.

[16] C. F. Melius, N. E. Bergan, and J. E. Shepherd, in *Twenty-Third Symposium (International) on Combustion* (The Combustion Institute, Pittsburgh, PA, Orleans, France, 1990).

INITIAL DISTRIBUTION

Dr. E. Fenton Carey, Jr.
U.S. Department of Energy (ST-60)
1000 Independence Avenue, S.W.
Room GA 155
Washington, DC 20585

Dr. Robert Marianelli
U.S. Dept. Of Energy
19901 Germantown Rd.
Germantown, MD 20874

Paul Maupin
ER-142
U.S. Dept. Of Energy
19901 Germantown Rd.
Germantown, MD 20874

Dr. Robert W. Holst
SERDP Program Office
Program Manager for Compliance and
Global Environmental Change
901 North Stuart Street, Suite 303
Arlington, VA 22203

Ed Ansell
US Army Defense Ammunition
Center
Attn: SMCAC-TD
Savanna, IL 61074-9639

Jenny Dowden
Labat-Anderson Incorporated
8000 Westpark Dr.
Suite 400
McLean, VA 22102

John Harrison
SERDP Program Office
901 North Stuart Street, Suite 303
Arlington, VA 22203

Jim Hurley
US AF AL/EQS
139 Barnes Drive, Suite 2
Tyndall Air Force Base, FL 32403

Richard Kirts
Naval Civil Engineering Laboratory
560 Laboratory Dr.
Port Hueneme, CA 93043-4328

Crane Robinson
Arament Research
Development & Engineering Center
(ARDEC)
SMCAR-AES-P
Building 321
Picatinny Arsenal, NJ 07806-5000

Dr. Peter Schmidt
Office of Naval Research
Chemistry Division
800 North Quincy Street
Arlington, VA 22217-5660

Dr. Regina E. Dugan
DARPA/DSO
3701 N. Fairfax Dr.
Arlington VA
22203-1714

Dr. Robert Shaw
Chemical & Biological Sciences Div.
U.S. Army Research Office
Research Triangle Park, NC 27709-2211

Prof. Martin A. Abraham
The University of Tulsa
Department of Chemical Engineering
600 South College Avenue
Tulsa, OK 74104-3189

Prof. Joan F. Brennecke
University of Notre Dame
Department of Chemical Engineering
Notre Dame, IN 46556

Dr. Kenneth Brezinsky
Dept. of Mechanical and Aerospace Engineering
Princeton University
PO Box CN5263
Princeton, NJ 08544-5263

Prof. Klaus Ebert
Kernforschungszentrum Karlsruhe
Institut fur Heisse Chemie
Postfach 3640
D-76021 Karlsruhe
Germany

Dr. Robert E. Huie
National Institute of Standards and Technology
Chemistry A261
Gaithersburg MD 20899

Prof. Earnest F. Gloyna
University of Texas at Austin
Environmental and Health Engineering
Austin, TX 78712

Prof. Keith Johnston
University of Texas at Austin
Chemical Engineering Dept.
26th and Speedway
Austin, TX 78712-1062

Prof. Micheal T. Klein
Chairman
University of Delaware
Chemical Engineering Dept.
Colburn Labs Academic Street
Newark, DE 19716-2110

Prof. Phillip E. Savage
University of Michigan
Chemical Engineering Department
Herbert H. Dow Building
Ann Arbor, MI 48109-2136

Prof. Jefferson W. Tester
Massachusetts Institute of Technology
Energy Laboratory
Room E40-455
77 Massachusetts Avenue
Cambridge, MA 02139

K.S. Ahluwalia
Foster Wheeler Development Corporation
Engineering Science & Technology
12 Peach Tree Hill Road
Livingston, NJ 07039

Armand A. Balasco
Arthur D. Little Inc.
Acorn Park
Cambridge, MA
02140-2390

Dr. Hiroshi Inomata
Tohoku University
Aoba Aramaki
Sendai 980
JAPAN

Thomas G. McGuinness
255 41st St.
Apt. 9
Oakland CA 94611

Carol A. Blaney
Kimberly-Clark
1400 Holcomb Bridge Rd.
Roswell, GA 30076-2199

Dr. David A. Hazelbeck
General Atomics
M/S 15-100D
3550 General Atomics Court
San Diego, CA 92121-1194

W. Killilea
General Atomics
3550 General Atomics Court
San Diego, CA 92121-1194

Richard C. Lyon
Eco Waste Technologies
2305 Donley Drive
Suite 108
Austin, TX 78758-4535

Dan Greisen
1940 Alabama Ave
PO Bxo 3530
Rancho Cordova, CA 95741-3530

Dr. Steven J. Buelow
CST-6
Los Alamos National Lab.
Los Alamos, NM 87545

Philip C. Dell'Orco
Los Alamos National Laboratory
Explosives Technology & Safety C920
Los Alamos, NM 87545

Dr. Albert Lee
NIST
Bldg. 221 Room B312
Gaithersburg, MD 20899

Dr. William Pitz
LLNL
P.O. Box 808 L-014
Livermore, CA 94551-0808

Prof. Jean Robert Richard
CNRS
Combustion Laboratory
1C Avenue de la Recherche Scient.
Orleans 45071
France

Dr. Gregory J. Rosasco
Nat'l Institute of Standards and
Technology
Division 836, Bldg. 221, Rm B-312
Gaithersburgh, MD 20899

MS0828 P. J. Hommert, 1503

MS0701 R. W. Lynch, 6100
MS0735 D. E. Arvizu, 6200
6203 A. P. Sylwester
6211 G. A. Carlson
6212 N. B. Jackson

MS0756 G. C. Allen, 6607

MS9001 T. O. Hunter, 8000
Attn: 8100 M. E. John
8200 L. A. West
8400 R. C. Wayne
8800 P. E. Brewer

MS9214 C. Melius, 8117

MS9054 W. J. McLean, 8300

MS9042 C. Hartwig, 8345

MS9051 L. Rahn, 8351

MS9055 F. Tully, 8353

MS9052 D. R. Hardesty, 8361 (2)

MS9052 S. W. Allendorf, 8361

MS9052 M. D. Allendorf, 8361

MS9052 L. L. Baxter, 8361

MS9052 S. G. Buckley, 8361

MS9052 M. M. Lunden, 8361

MS9052 T. A. McDaniel, 8361

MS9052 D. K. Ottesen, 8361

MS9052 C. Shaddix, 8361

MS9052 J. Aiken, 8361

MS9052 E. Croiset, 8361

MS9052 R. Hanush, 8361

MS9052 S. Rice, 8361 (20)

MS9053 R. Carling, 8362

MS9053 R. Steeper, 8362

MS9053 R. Gallagher, 8366

MS9101 B. Peila, 8411

MS9105 T. T. Bramlette, 8422

MS9105 J. Lipkin, 8419

MS9406 B. Haroldsen, 8412

MS9406 H. Hirano, 8412

MS9406 C. LaJeunesse, 8412

MS9406 M. C. Stoddard, 8412

MS9007 J. Swearengen, 8419

MS9404 B. Mills, 8713